Cellulose nanofibril foams: Links between ice-templating conditions, microstructures and mechanical properties

F. Martoïa [a,b,c,d,e], T. Cochereau [a,b,c,d,e], P.J.J. Dumont [a,b,c,*], L. Orgéas [d,e], M. Terrien [a,b,c], M.N. Belgacem [a,b,c]

[a] Univ. Grenoble Alpes, LGP2, F-38000 Grenoble, France
[b] CNRS, LGP2, F-38000 Grenoble, France
[c] Agefpi, LGP2, F-38000 Grenoble, France
[d] Univ. Grenoble Alpes, 3SR Lab, F-38000 Grenoble, France
[e] CNRS, 3SR Lab, F-38000 Grenoble, France

ARTICLE INFO

ABSTRACT

This study aimed at investigating how ice templating conditions affected the shrinkage, the microstructure, and the mechanical properties of cellulose nanofibril (NFC) foams. Enzymatic and TEMPO-oxidized NFC foams were fabricated using two solidification techniques, i.e., quenching NFC suspensions in temperature-controlled baths, and mechanical stirring of NFC suspensions during solidification followed by quenching, prior to freeze-drying. Foams prepared by direct quenching using stabilized TEMPO-oxidized NFC suspensions exhibited higher specific mechanical properties and more regular anisotropic cells with unimodal size than enzymatic NFC foams. In addition, NFC concentration and NFC morphology severely affected the foam shrinkage and the geometry of foam cells. Controlling the solidification had also a drastic effect on the foam microstructure, e.g. foams prepared by mechanical stirring and quenching exhibited bimodal cell size and enhanced mechanical properties. The compressive behavior of foams showed successive elastic, strain-hardening and densification regimes with auxetic effects and strain localization. Both the elastic modulus and the yield stress were power-law functions of the foam relative density whose exponents reached unusual high values for enzymatic NFC foams, potentially because of their chaotic microstructures. The evolution of a typical TEMPO-oxidized NFC foam was studied under compression using X-ray microtomography, unveiling deformation mechanisms at the cell scale.

© 2016 Elsevier Ltd. All rights reserved.

1. Introduction

Cellulose nanofibrils (NFCs) are the elementary reinforcing constituents of plant cell walls [1–3]. NFCs can be extracted in the form of aqueous colloidal suspensions by subjecting slurries of cellulose fibers to strong mechanical disintegration processes [4–5]. However, several pre-treatments of cellulose fibers such as enzymatic hydrolysis [6–7] or chemical oxidation by a 2,2,6,6-tetramethylpiperidine-1-oxyl radical (TEMPO)-mediated system [8–9] are often used prior to the mechanical treatments to reduce energy consumption and make cellulose nanofibrils more uniform in size. The resulting NFC suspensions can be used to manufacture a variety of promising renewable materials such as foams [10–14] and aerogels [15–16], films and nanopapers [17], with interesting specific physical and mechanical properties. NFC foams and aerogels constitute low density (density ranging from 1 kg m^{-3} to 100 kg m^{-3}) bio-based materials with high mechanical and insulation properties (elastic modulus: 10^{-2} MPa ≤ E ≤ 5 MPa and

thermal conductivity: 18 mW K^{-1} m^{-1} ≤ λ ≤80 mW K^{-1} m^{-1}) and with a great potential in several engineering fields [11,13,18–20]. They can be used in the automotive industry as heat and/or sound insulation boards [18–20] or for biomedical applications as filtering and purifying membranes [21–23] or even as scaffolds [24] for tissues. However, the selection and the use of a specific foam for a particular engineering application require a proper understanding and control of its microstructure and mechanical behavior, particularly, in terms of deformation and related damage mechanisms [25–26].

NFC aerogels of ultra low density and with nanometric pore sizes are generally fabricated using supercritical drying techniques [16]. In contrast, NFC foams with micrometric cell sizes can be obtained from NFC water suspensions by ice templating, i.e., after freezing of suspensions and sublimation of the formed ice crystals (freeze-drying) [11–13] or by simple ambient drying (water evaporation) from surface-modified cellulose nanofibril suspensions [27] Ice templating process [28–32] has received considerable attention in recent years owing to its simplicity and to the wide variety of porous materials that this technique can provide. This technique can also be used to obtain hierarchically structured composite foams with interesting physical properties [13,18–20,33] from aqueous dispersions of cellulose nanofibrils and polymers or fillers (clay, graphene oxide, montmorillonite).

However, the control of the arrangement and organization of solid particles during the water solidification phase is complex and still not well understood [28–30]. For example, particle segregation and separation induced by ice growth in aqueous colloidal suspensions depend on a large number of factors related both to the processing conditions (*e.g.* temperature field) and the nature of colloids [14,28–32] (particle size, geometry, density, conductivity, surface charge density and impurities). If these phenomena and their effects on the microstructures and mechanical performances on the fabricated foams have been investigated for many ice-templated systems [28–32] much less is known concerning NFC systems:

- NFC foams were often prepared using quenching processing routes with temperatures and cooling rates that varied over narrow ranges [34–38]. The solidification or freezing of NFC water suspensions was usually achieved by dipping them into liquid nitrogen baths or by placing them inside freezers. To the best of our knowledge, the effect of quenching temperature on the microstructure and mechanical properties of NFC foams has not been extensively investigated.
- Some recent studies investigated the effect of the freezing direction on the structural characteristics and mechanical properties of NFC foams [13–14,20,39]. For instance, Jee et al. [14] fabricated NFC foams using a specially designed unidirectional freezing device. Foams that were prepared using this technique exhibited lamellar channel structures oriented parallel to the freezing direction. At a finer scale, Menier et al. [39] showed using X-ray diffraction techniques that unidirectional freezing of NFC suspensions produced cellular foams with high alignment of the particles in the freezing direction. The authors also observed that the degree of orientation decreased with increasing the NFC concentration.
- Some studies also investigated the effect of NFC concentration on the structural and mechanical properties of NFC foams. For example, using enzymatic NFCs, Sehaqui et al. [11] showed that increasing the NFC concentration from 0.7 to 10 wt% yielded denser foams ($7 \, \text{kg m}^{-3} \leq \rho \leq 103 \, \text{kg m}^{-3}$) with finer cellular architectures. In addition, the authors found that both the compression modulus and yield stress were power-law functions of the NFC foam density with power-law exponents $n = 2$ and $m = 1.5$, respectively. However, the effect of the suspension nature, namely the colloidal stability and the morphology of NFCs on the microstructure and mechanical properties of the obtained NFC foams has not yet been studied. The preparation of NFC foams by quenching or unidirectional freezing and ice sublimation is easy to operate but usually leads to anisotropic foam microstructures because of the radial and columnar growth of ice crystals during freezing [13–14,20,28–33,39–40]. This technique does not enable materials with multiple scales of porosity to be obtained since the final architecture is induced by a unique physical mechanism that involves the segregation and redistribution of NFCs by the moving ice front [28–30]. To date, no study attempted to obtain foam cells with globular and/or multimodal morphology from NFC systems. However these types of foams could exhibit very interesting mechanical properties [41]. To obtain the aforementioned foam cell structures, several nucleation processes or mechanisms are required during foaming [28,41].

Thus, the objectives of this study were to investigate the effect of processing conditions and NFC suspension properties (surface charge density, NFC morphology and concentration) on the microstructural and mechanical properties of NFC foams. Two types of NFC water suspensions, namely enzymatic and TEMPO-oxidized NFC suspensions were used. Both NFC suspensions were quenched at different freezing temperatures ($-114 \,°\text{C} \leq T \leq -10 \,°\text{C}$) that enabled the cooling rate to be varied over a wide temperature range. An original 'sorbet-like' solidification technique was also used to investigate the effect of mechanical stirring on the structure and the mechanical properties of NFC foams.

The microstructure of the obtained NFC foams was investigated using both electron microscopy and synchrotron X-ray microtomography. Their mechanical properties were evaluated using both standard compression experiments and compression tests with 3D *in situ* observations using high resolution X-ray synchrotron microtomography. To the best of our knowledge, these experiments are original and have never been used to characterize NFC foam cell structures and their deformation micromechanisms.

2. Materials and methods

2.1. Extraction of NFC suspensions

TEMPO-oxidized NFC suspensions at a concentration of 0.75%wt were extracted from a commercial eucalyptus bleached kraft pulp supplied by Celbi (Portugal) using the experimental procedure reported by Martoïa et al. [42]. Enzymatic NFC suspensions at a concentration of 2 wt% were supplied by Centre Technique du Papier (Grenoble, France). These suspensions were isolated from an enzymatically treated birch bleached kraft pulp by mechanical disintegration using a homogenizer M-110 EH-30 (GEA Niro Soavi, Parma, Italy). To prepare NFC foams with various relative densities ρ/ρ_s ($\rho_s = 1500 \, \text{kg m}^{-3}$ is the density of cellulose [43]), both types of suspensions were either diluted by adding deionized water, or concentrated by high speed centrifugation (10,000 rpm for 20 min). Hence, TEMPO-oxidized and enzymatic NFC suspensions at various concentrations c that ranged from 0.1 to 1.65 and 0.7 to 7.5 wt% were prepared, respectively (corresponding to NFC volume fraction ϕ that ranged from 0.0007 to 0.011 and 0.0047 to 0.05, respectively). All the as-prepared NFC suspensions were at pH 7.5–8.

2.2. Processing of NFC foams

2.2.1. Direct quenching

In a first approach, NFC foams were prepared using direct quenching (Fig. 1a). This technique consisted in pouring 5 ml of NFC suspensions into cylindrical glass tubes of diameter $D_t = 16$ mm and length $L_t = 42$ mm. Then, the tubes were quenched in various baths having a volume V of ≈ 300 ml, *i.e.*, baths with various liquids at their solid-liquid transition temperature (Fig. 1a). These liquids enabled the temperature of the baths and the averaged cooling rate of the NFC suspensions to be easily controlled (Table 1). Photographs of the upper surface of the NFC suspensions during freezing (Fig. 1a) showed that away from the bottom of the tubes, the ice front homogenously moved in the radial e_r-direction. Furthermore, ice formation induced a positive volume variation and caused the suspension to flow in the vertical e_z-direction of the tube. This vertical displacement was at the origin of the 'conical parts' that were visible on the top of NFC foams. Note that in the investigated range of quenching temperatures, no macroscopic cracks or splits were observed while freezing NFC suspensions. At the end of the solidification process, frozen suspensions were dried in a freeze-dryer Alpha 2-4LD plus (Christ, Osterode am Harz, Germany) for 48 h. The temperature of the inner chamber of the freeze-dryer was set to $-60 \,°\text{C}$ and the pressure to 20 mbar. All the NFC concentrations c that were used with this quenching procedure, the density ρ and relative density ρ/ρ_s of the corresponding NFC foams are given in Table 2.

2.2.2. Mechanical stirring and quenching

We also investigated an alternate freezing processing route inspired from the food industry or the metallurgy to process metals for thixocasting [44–45]. The adopted technique consisted in restraining, with a mechanical stirring, the dendritic and columnar ice crystal growth during solidification to obtain a first class of ice grains with globular shape. Hence, NFC suspensions were poured into a sorbet machine (Domoclip DOM 147P) and then continuously mixed at 35 rpm
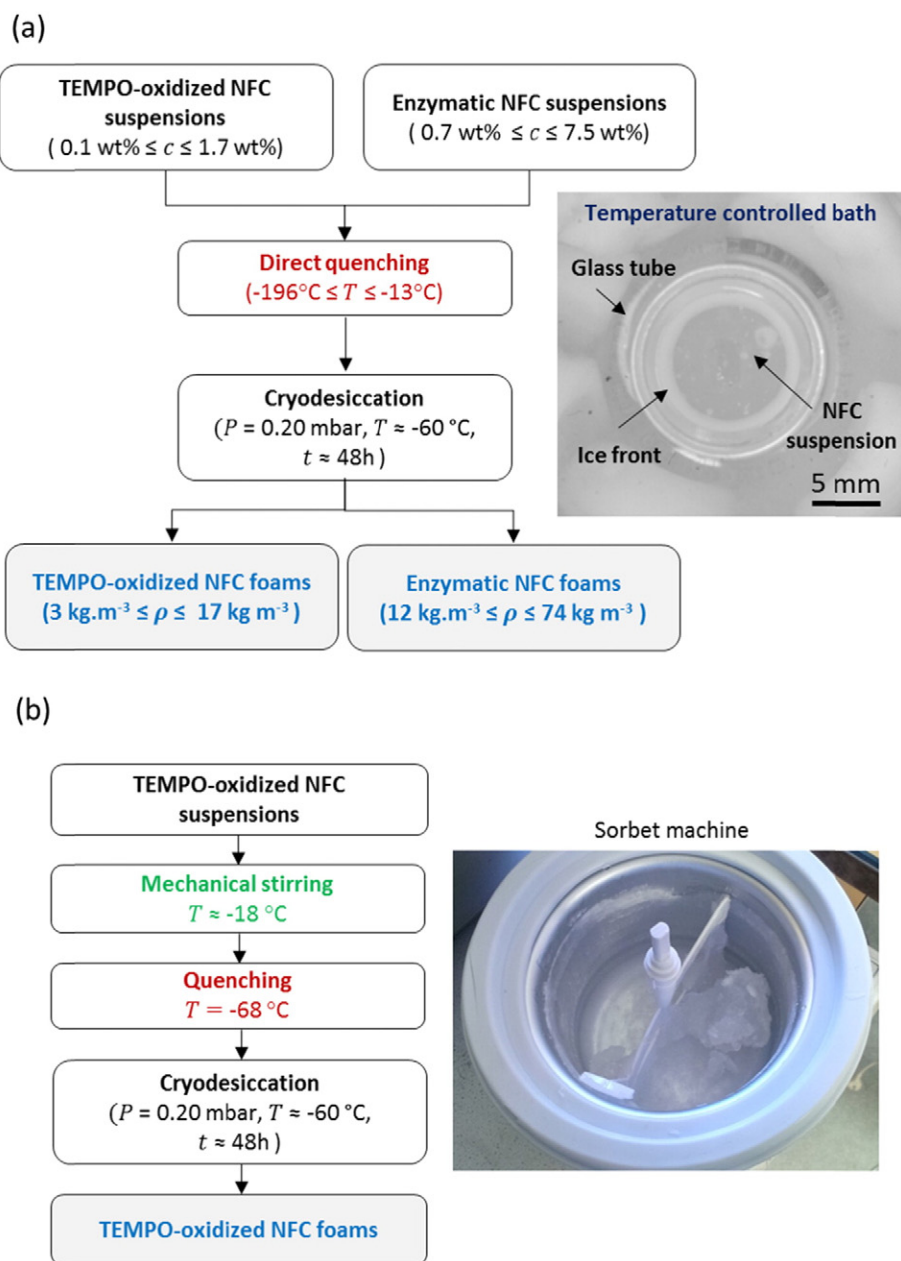
(a)

(b)

Fig. 1. (a) Schematic representation of the direct quenching procedure used to obtain enzymatic and TEMPO-oxidized NFC foams. (b) Sketch of the 'sorbet-like' NFC foam processing route.

and at −18 °C until the suspensions exhibited ice-cream textures (≈1 h) (Fig. 1b). Then, glass tubes were filled with 5 ml of the ensuing suspensions before being quenched in a butyl-acetate bath at a temperature of −68 °C to completely solidify the suspensions.

Table 1
Liquids used to freeze NFC suspensions. All the chemicals were provided by Sigma Aldrich (France) and used without any further purification.

Cooler	Temperature of the solid-liquid bath (°C)	Total solidification duration (min)
Benzonitrile	−13	≈20
Acetonitrile	−40	≈8
Butyl acetate	−68	≈6
Acetone	−80	≈5
Propanol	−100	≈4
Ethanol	−114	≈3

2.3. Microstructure characterization

2.3.1. NFC suspensions

The meso-, micro- and nano-scale morphologies of NFCs and NFC suspensions were investigated using various optical and electronic imaging techniques. The homogeneity of the processed NFC suspensions was first assessed from photographs that were taken using a 36.2 megapixel camera (Nikon D800) equipped with a 10-mm macro lens. Then, optical micrographs were recorded in transmission mode on NFC aqueous suspensions diluted to 0.1 wt%, using an optical microscope (Axio Imager M1 m, Zeiss) equipped with a camera (AxioCAM MRC5, Zeiss). AFM observations were also performed to analyze the nanoscale morphology of NFCs. AFM specimens were prepared by depositing a drop of NFC suspension at a concentration of 0.001 wt% onto freshly-cleaved mica substrates. Then, these specimens were air-dried for few minutes before being imaged using an atomic force microscope (Nanoscope III®, Veeco, Canada) in tapping mode with a silicon

Table 2

Concentrations c of the NFC suspensions used to fabricate by direct quenching NFC foams. The density ρ and the relative density ρ/ρ_s of the resulting foams are also reported (note that the foam porosity is equal to $1 - \rho/\rho_s$). Note also that it was difficult to accurately estimate the density of some foams, *i.e.*, those prepared using the less concentrated NFC suspensions, because of their very irregular shapes.

	c (wt%)	ρ (kg m^{-3})	ρ/ρ_s
TEMPO NFCs	0.1	–	–
	0.15	–	–
	0.2	3	0.002
	0.5	4.5	0.003
	0.55	6.2	0.004
	0.8	8.5	0.006
	1.2	11	0.0075
	1.4	14.1	0.0095
	1.65	17	0.012
	7.5	74	0.053
	4.5	48	0.035
	3	33	0.024
Enzymatic NFCs	2.2	23.5	0.017
	1.5	17.5	0.013
	1	12.5	0.009
	0.7	–	–

cantilever (OTESPA®, Bruker, USA) at different locations over scanning areas of 3 μm × 3 μm.

2.3.2. NFC foams

The microstructural properties of NFC foams were investigated at different scales using a scanning electron microscope equipped with a field emission gun (FEG) system (Zeiss Ultra 55 gemini column) in low vacuum conditions and with a voltage set at 2 kV. Sample preparation is crucial to obtain representative images of foam cell structures. Thus, NFC foams were carefully cut in the horizontal plane using razor blades. Before taking the images, a layer of gold and palladium with a thickness of 2–3 nm was deposited onto the surface of the samples. The radial pore size of NFC foams was then roughly estimated from the FE-SEM micrographs using the image analysis freeware ImageJ.

The NFC foam microstructures were also finely characterized using 3D X-ray microtomography. These experiments were performed using the high-resolution X-ray synchrotron microtomograph of the ID 19 beamline at the European Synchrotron Radiation Facilities (Grenoble, France). This beamline was chosen because it delivered an intense coherent and monochromatic X-ray source and enabled images with a high signal-to-noise ratio to be acquired [46–47]. The X-ray beam energy was set to 19 keV and a voxel size of 0.32^3 μm^3 was chosen to obtain accurate representations of the foam cell structures. The foam samples were fixed on a rotation stage between the X-ray source and the detection unit that recorded the transmitted X-rays. Samples were rotated under the beam incrementally up to 180° to provide a set of 3000 radiographs (duration of the scan ≈ 60 s). Then, 3D images were reconstructed using the so-called Paganin procedure, which is based on using the phase contrast in the images [48–49].

2.4. Mechanical characterization of NFC foams

2.4.1. Macroscale compression tests

Uniaxial compression tests were performed on cylindrical specimens (mean diameter $D \approx 16$ mm and mean initial height $h_0 \approx 15$ mm). Before testing, all NFC foams were stored for at least one day in controlled conditions ($T = 25$ °C and r.h. = 56%). NFC foams were then subjected to four successive load-unload cycles and at a constant compression strain-rate of $|\dot{\varepsilon}| \approx 0.002$ s^{-1} with increasing the compression strain ε upon loading. These experiments were performed using an electromechanical testing machine (Instron 5960, France) equipped with a force sensor of 50 N or 5 kN (depending on

the relative density of the considered foam). During the experiments, both the nominal compression stress $\sigma = F/S_0$ (where F is the normal force and S_0 the initial cross section area of the foam) and the logarithmic strain $\varepsilon = \ln(h/h_0)$ were acquired (h is the current height of the foam). It was checked that the stiffness of the entire testing device was much higher than those of NFC foams, so that ε was considered to be a relevant macroscale axial deformation of samples. As suggested by Gibson and Ashby [25], the apparent compression modulus E of the foams was estimated from the initial linear part of the $\sigma - \varepsilon$ curves, *i.e.*, typically between $0 < \varepsilon < 0.05$ (Fig. 7). The apparent yield stress σ_y was calculated from the intersection of the two tangent lines parallel to the apparent elastic domain and the nearly linear strain hardening plasticity regime above the yield stress (Fig. 7).

2.4.2. In situ compression test with X-ray synchrotron microtomography

The microstructure of a typical TEMPO-oxidized NFC foam, which was obtained using a quenching temperature of −13 °C, and its evolution under compression loading were studied using X-ray synchrotron microtomography. For that purpose, the foam was cut in a small cube ($\approx 4 \times 4 \times 4$ mm^3) and then subjected to low a strain-rate compression tests ($|\dot{\varepsilon}| = 0.005$ s^{-1}), using a specially designed micro-compression machine [50] (see supplementary information). The compression test was interrupted at three compression strains of $\varepsilon = 0.11, 0.8$ and 2.2. In the undeformed configuration and for each compression stop, a fast scan (duration ≈ 60 s) of the NFC foam was first performed using a voxel size of $1.6 \times 1.6 \times 1.6$ μm^3 to visualize the entire sample. In addition, to obtain an accurate representation of the bulk deformation and failure micro-mechanisms that occurred at the cell scale, the foam was also imaged using a smaller voxel size of $0.32 \times 0.32 \times 0.32$ μm^3, by performing and concatenating four additional high resolution scans along the entire height of the sample.

3. Results

3.1. Microstructures of the parent NFC suspensions

The photographs in Fig. 2a show that enzymatic NFC suspensions exhibited spatially heterogeneous mesoscale textures such as flocs (50–100 μm) [42]. On the contrary, TEMPO-oxidized NFC suspensions did not exhibit this type of mesoscale structures [42,51–52] (Fig. 2b). These suspensions were transparent, stable and non-flocculated. The origin of this difference was related to the surface charge density of NFCs. Indeed, the content of carboxyl groups (–COOH) determined by conductimetric titration was 1.45 mmol g^{-1} for NFCs obtained after TEMPO-mediated oxidation [42], whereas it was only 0.075 mmol g^{-1} for enzymatic NFCs. At pH 8, *i.e.*, close to the pKa of the acid-base pair (pKa ≈ 8.5), carboxyl groups were partially dissociated into carboxylate groups. Thus, TEMPO-oxidized NFCs were much more electrostatically charged and kinetically stable in water suspension than enzymatic NFCs [42,52].

Fig. 2c, e show that enzymatic NFC suspensions were polydisperse suspensions that contained few partially fibrillated fibers (diameter ≈ 20 μm and length ≈ 150–300 μm), bundles of fibrils having a diameter that ranged between 100 and 500 nm, and finer elements in the form of fibril aggregates with a diameter that ranged between 20 and 50 nm. In contrast, the polydispersity of TEMPO-oxidized NFCs was much smaller. These suspensions contained few fibers that had dimensions that were close to those of the original fibers (diameter ≈ 20 μm and length ≈ 600–700 μm) and much more very slender individualized and kinked fibrils with a diameter and length that ranged between 3 and 5 nm and between 1 and 1.4 μm, respectively (Fig. 2d, f) [42,52]. However, it is worth noting that complex challenges are still encountered in the precise determination of the size of the extracted NFCs [53–54].
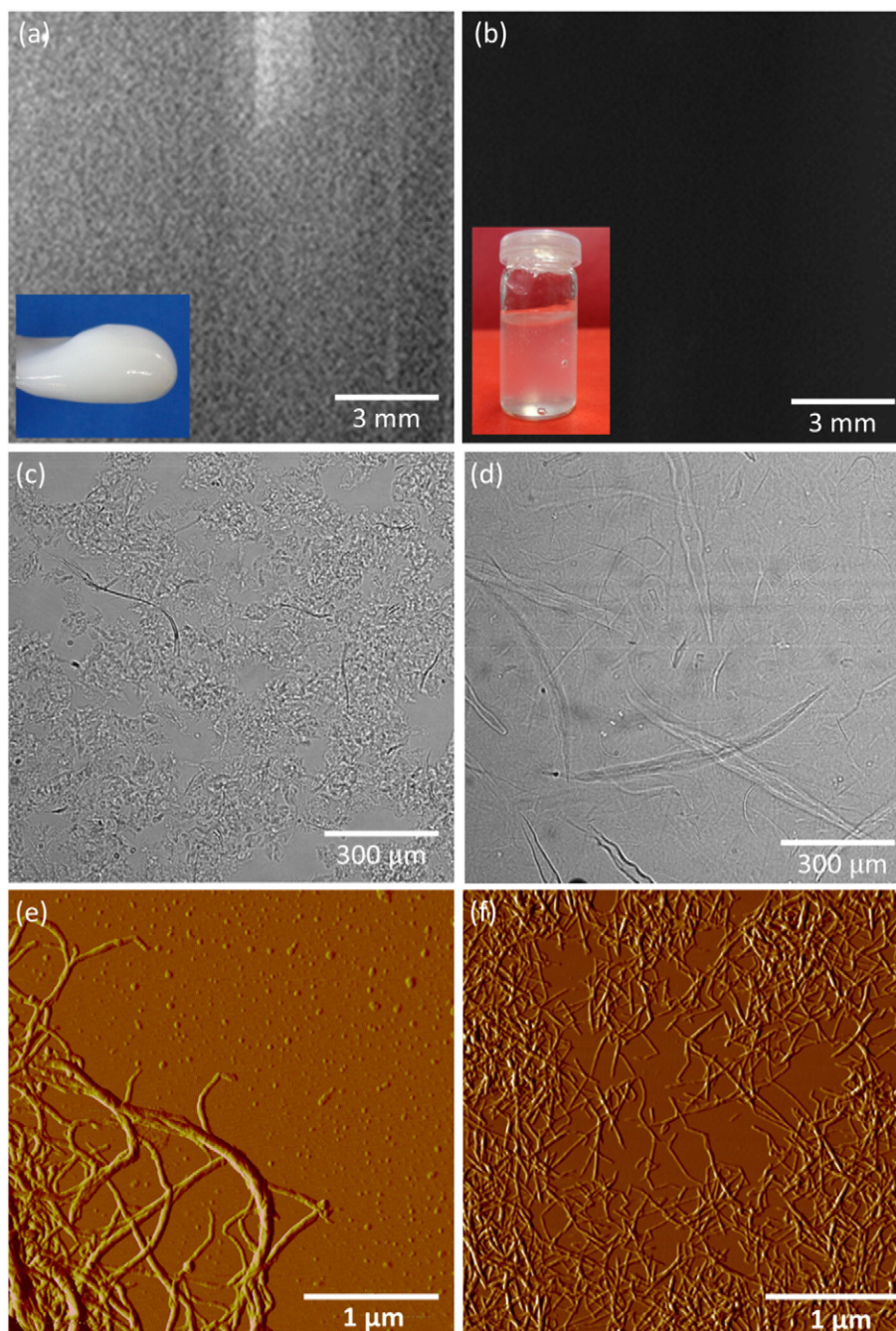
Fig. 2. Photographs obtained with a black background of a 2-wt% enzymatic NFC suspension (a), and a 0.75-wt% TEMPO NFC suspension (b). Optical micrographs of a 0.1-wt% enzymatic NFC suspension (c), and a 0.1 wt% TEMPO-oxidized NFC suspension (d). AFM micrographs of an enzymatic NFC film (e) and TEMPO NFC film (f).

3.2. Shrinkage of NFC foams: effect of the NFC suspension type and concentration

An analysis of the geometry of the produced foam samples was first conducted. For both types of suspensions, decreasing the NFC concentration c yielded an increase in the sample diameter shrinkage (Fig. 3). Above a critical NFC concentration c^*, i.e., $c^* \approx 1$ wt% for enzymatic NFC suspensions (Fig. 3a) and $c^* \approx 0.2$ wt% for TEMPO-oxidized NFC suspensions (Fig. 3b), the diameter reduction was limited and the samples practically exhibited cylindrical shapes. In contrast, a sharp reduction of the foam diameter and a degradation of the sample cylindrical shape were observed below this critical concentration c^*.

3.3. Microstructures of NFC foams

In Figs. 4 and 5, SEM micrographs and 3D tomographic images show that both TEMPO-oxidized and enzymatic foams exhibited complex cellular architectures and open porosity. The morphology of the cells was different from that usually observed in most of the synthetic polymer foams [25–26]. NFC foams consisted of irregular arrangements of thin plates (in the form of NFC films or nanopapers) that occasionally intersected with remaining partially fibrillated fibers or dangling mass, i.e., unconnected branches (see the comments related to Fig. 2c, d and SEM micrographs in Fig. 4a). For TEMPO-oxidized foams, 3D views show that the plates were slightly curved
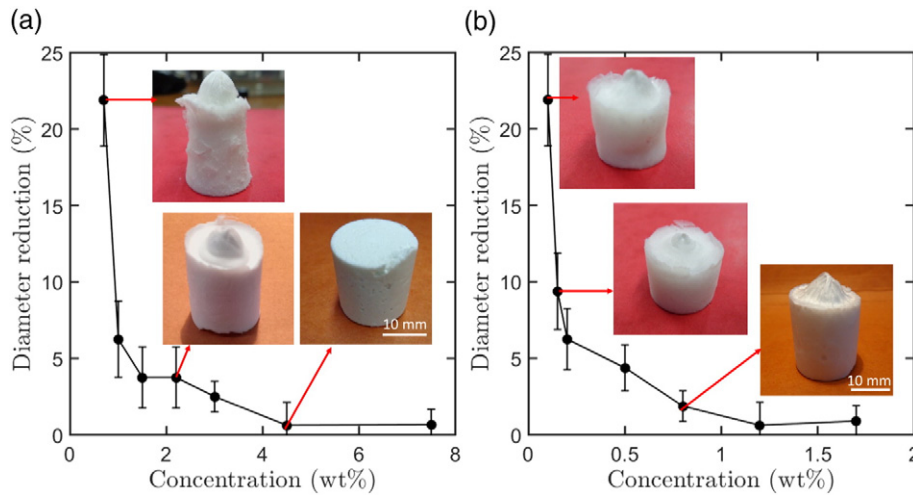
Fig. 3. Graphs (a,b) show the evolution of the mean diameter reduction $(D_t - D)/D_t$ (where D_t is the diameter of the tube and D is the mean diameter along the height of the foam samples) as a function of the NFC concentration for (a) enzymatic NFC suspensions and (b) TEMPO-oxidized NFC suspensions. These foams were prepared by direct quenching using a freezing temperature $T \simeq -68$ °C.

(Fig. 4e, f). Their in-plane dimensions and their thickness also varied over the plate surface (Fig. 4e, f) but also from one plate to another (Figs. 4 g,h and 5 f,h). In addition, TEMPO-oxidized and enzymatic NFC foams exhibited remarkable microstructural differences. The geometry of TEMPO-oxidized cell foams (Fig. 4) was more regular compared with that of enzymatic foams (Fig. 5). The 2D X-ray and the SEM images in Fig. 4 also show the anisotropic and columnar geometry of the pores. In general, three cell walls meet at each edge with interface angles that varied over a wide range (Fig. 4e, f). On the contrary, enzymatic foams exhibited more chaotic and intricate structures, which made difficult the direct observations of the foam cell geometry (Fig. 5).

As shown by the multiscale images in Figs. 4 and 5, the morphology of the pores/cells varied drastically as a function of the applied freezing temperature. Between −13 °C and −80 °C, the radial pore size decreased from few hundred microns (300–50 μm) to a few tenths of microns (20–10 μm) for TEMPO-oxidized and enzymatic foams. Note also that NFC foams obtained at high freezing temperature, *i.e.*, $T = -13$ °C (Fig. 4a, e–h), consisted of cells that were more polydisperse compared with those observed in NFC foams that were obtained at lower freezing temperature (Fig. 4b). Further, between −80 °C and −114 °C, no significant variation in the pore morphology and size was evidenced from the SEM micrographs. Similar noteworthy variations in the pore morphology have also been reported by Jiang et al. [55] who fabricated TEMPO-oxidized foams using two different freezing temperatures, *i.e.*, $T = -20$ °C and $T = -196$ °C.

SEM and X-ray micrographs in Fig. 5c–f show the influence of NFC concentration on the microstructural properties of enzymatic NFC foams. Denser NFC foams exhibited finer cellular architectures. Similar observations have been reported by Sehaqui et al. [11] for enzymatic NFC foams. Note that we made similar observations for TEMPO-oxidized NFC foams. In addition, the 2D X-ray cross section views in Fig. 5f, h indicate that denser foams exhibited a larger number of walls/plates with thick cross sections.

Finally, Fig. 6 shows a collection of micrographs that were obtained for TEMPO-oxidized NFC foams ($\rho \approx 17$ kg m^{-3}, *i.e.*, $\rho/\rho_s \approx 1.2\%$) prepared using mechanical stirring followed by quenching. The resulting foams exhibited interesting bimodal structures that consisted of near-spherical mesoscale pores/cells with a diameter that ranged from 100 μm to 600 μm. These cells were flanked by more finer and anisotropic pores/cells in the form of 'buttresses' with dimensions that ranged between 20 and 50 μm. Note also that the fine pores shown in Fig. 6c exhibited slightly smaller dimensions compared with those observed in the foams that were prepared by direct quenching at the

same mean relative density (Fig. 6d). In accordance with the aforementioned comments on the influence of the NFC concentration on the stabilization of the foam shrinkage, this could be related to the concentration of NFC suspensions before freezing, which was locally higher using mechanical stirring than direct quenching.

3.4. Mechanical properties of NFC foams

3.4.1. Macroscale and mesoscale behavior

The compression stress-strain curves obtained for TEMPO-oxidized and enzymatic foams (Fig. 7) were typical of many elasto-viscoplastic cellular materials [25–26], with three distinct regimes:

- For $0 \leq \varepsilon \leq 0.07$, the NFC foams exhibited an initial practically linear behavior characterized by an apparent modulus E up to an initial yield stress σ_y.
- Above σ_y, the plastic deformation was marked, *i.e.*, with pronounced residual strain upon unloading. In this regime, the consolidation of foams occurred [25] and the stress was an increasing function of the compression strain. It is also worth noting that the unloading curves exhibited marked non-linear portions, showing that the elastic energy stored within the cell walls upon loading was sufficient to unfold them partially upon unloading.
- At higher compressive strains ($\varepsilon \geq 0.8$), all the curves exhibited a densification regime characterized by a sharp increase in the compressive stress σ.

The image insets in Fig. 7 are instructive. They show that below a macroscale compression strain of $\varepsilon = 0.25$, the sample deformations were practically homogeneous with auxetic effects that were characterized by a negative lateral strain (negative Poisson ratio ν). Above this strain, the sample deformations became heterogeneous with localized striction phenomena. Using the images that were recorded during the two tests shown in Fig. 7 (using a CCD camera Jai Pulnix RM-4200GE with a spatial resolution of 2048 × 2048 pixels) and analyzed using the procedure reported by Rodney et al. [56] to measure locally the axial and lateral compression strains, we found that for $0 \leq \varepsilon \leq 0.2$, TEMPO-oxidized and enzymatic foams shown in Fig. 7 exhibited Poisson's ratios ν that were close to −0.15.

3.4.2. Effect of relative density – Scaling laws

For both types of NFCs and foams which were prepared using a quenching temperature of −68 °C, the evolutions of the apparent
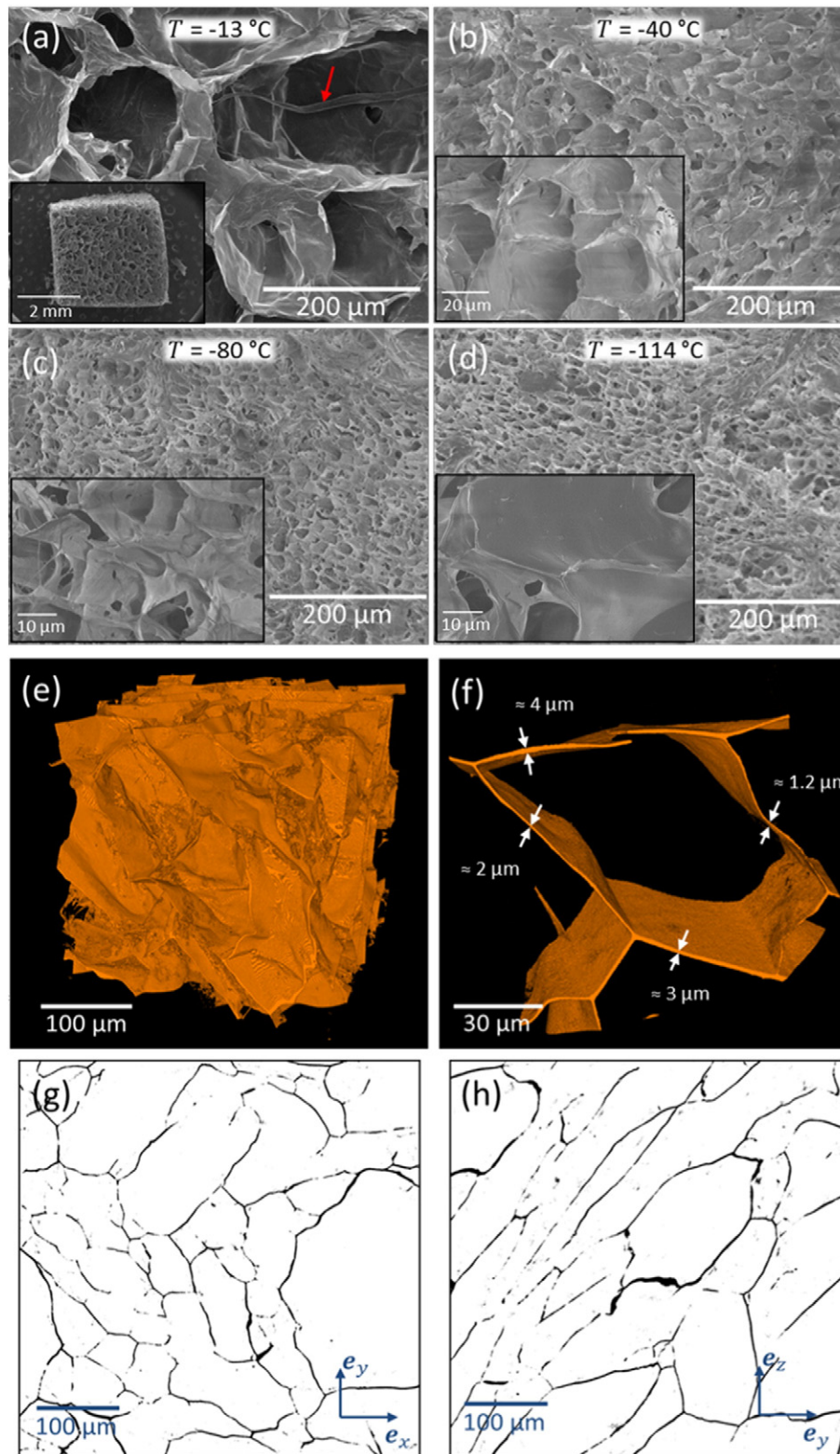
Fig. 4. (a–d) SEM-FEG micrographs of TEMPO-oxidized NFC foams ($\rho \approx 11$ kg m^{-3}, *i.e.*, $\rho/\rho_s \approx 0.75\%$) obtained after freezing at various temperatures and then freeze-dried. The red arrow in Panel a indicates a remaining fiber that was partially fibrillated/disintegrated. (e–f) 3D-rendered perspective views (voxel size: 0.32^3 µm^3) and (g–h) cross sections of a TEMPO-oxidized NFC foam ($\rho \approx 11$ kg m^{-3}, *i.e.*, $\rho/\rho_s \approx 0.75\%$, freezing temperature $T = -13$ °C) obtained using X-ray synchrotron microtomography.

modulus E and yield stress σ_y were plotted in Fig. 8a, b as a function of the foam relative density ρ/ρ_s. These figures show that E and σ_y were both power-law functions of ρ/ρ_s, *i.e.*, $E \propto (\rho/\rho_s)^n$ and $\sigma_y \propto (\rho/\rho_s)^m$, with power-law exponents $n = 2.29$ and 3.11, and $m = 2.22$ and 3.04 for

TEMPO-oxidized and enzymatic NFC foams, respectively. It is also worth to note that for a given relative density, the specific modulus and yield stress of the TEMPO-oxidized NFC foams were much higher than for the enzymatic NFC foams.
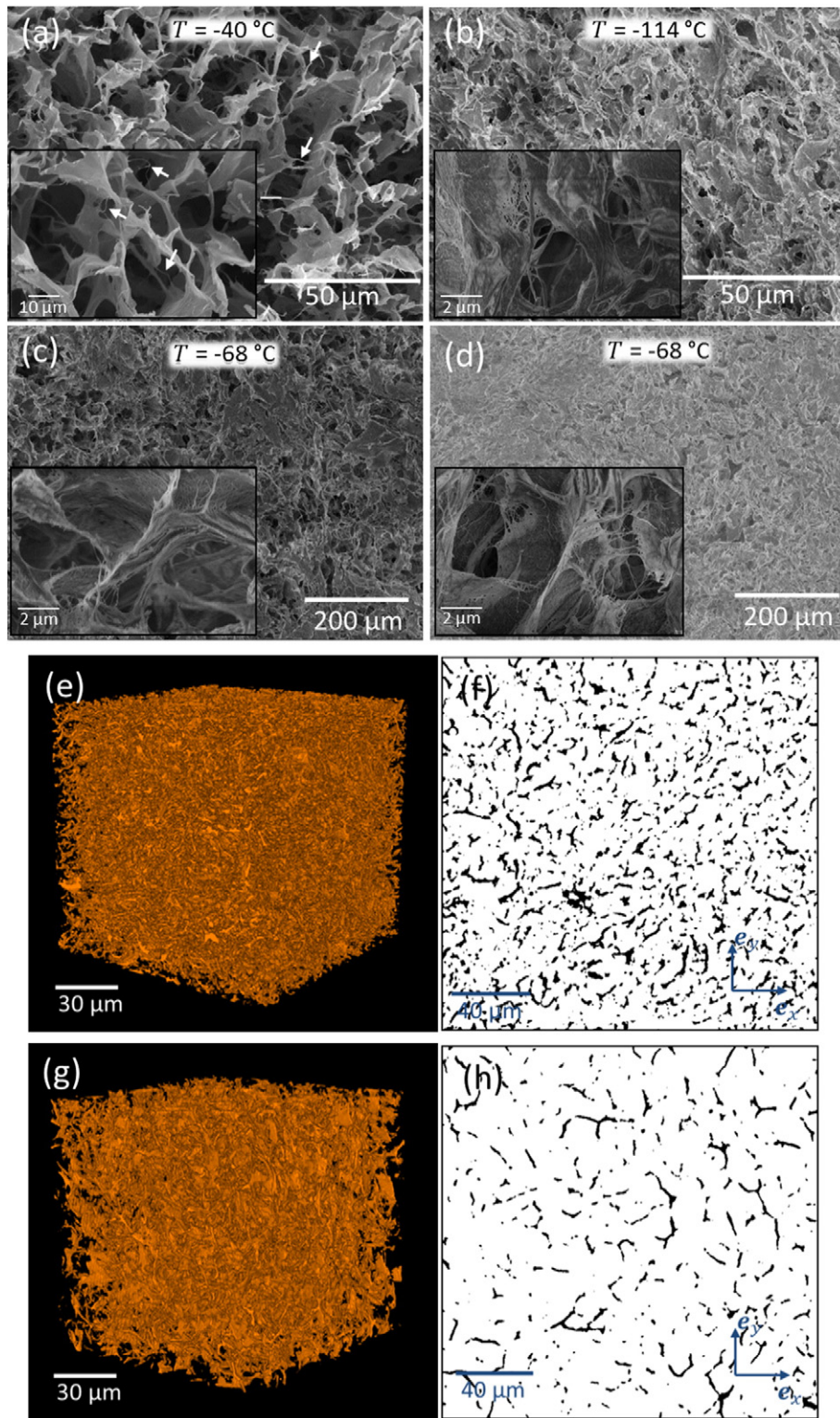
Fig. 5. (a–b) SEM-FEG micrographs of enzymatic NFC foams ($\rho \approx 23$ kg m^{-3}, *i.e.* $\rho/\rho_s \approx 1.7\%$) obtained after freezing at various temperatures and then freeze-dried. The white arrows in Panel a show some dangling branches. Enzymatic NFC foams with $\rho \approx 23$ kg m^{-3} ($\rho/\rho_s \approx 1.7\%$) (c), and $\rho \approx 48$ kg m^{-3} ($\rho/\rho_s \approx 3.5\%$) (d) obtained after freezing at $T = -68$ °C and then freeze-dried. (e, g) 3D-rendered perspective views (voxel size: 0.32^3 µm^3) and (f, h) cross section of segmented micrographs of enzymatic NFC foams ($\rho \approx 23$ kg m^{-3}, *i.e.*, $\rho/\rho_s \approx 1.7\%$, freezing temperature $T = -68$ °C) obtained using X-ray synchrotron microtomography.

3.4.3. Microscale deformation mechanisms of TEMPO-oxidized foams

The compression experiment that was performed using 3D *in situ* observations enabled deformation and failure mechanisms at the foam cell scale to be unveiled for one typical TEMPO-oxidized foam ($\rho/\rho_s \approx$ 0.75% and a quenching temperature of -13 °C). The corresponding stress-strain curve (Fig. 9) shows that, at the beginning of the test ($0 \leq \varepsilon \leq 0.15$), the mechanical response was similar to that obtained using larger cylindrical samples outside the microtomograph with the same foam (Fig. 7). The apparent compression modulus $E \approx 65$ kPa and yield stress $\sigma_y \approx 6$ kPa were consistent with those obtained using larger

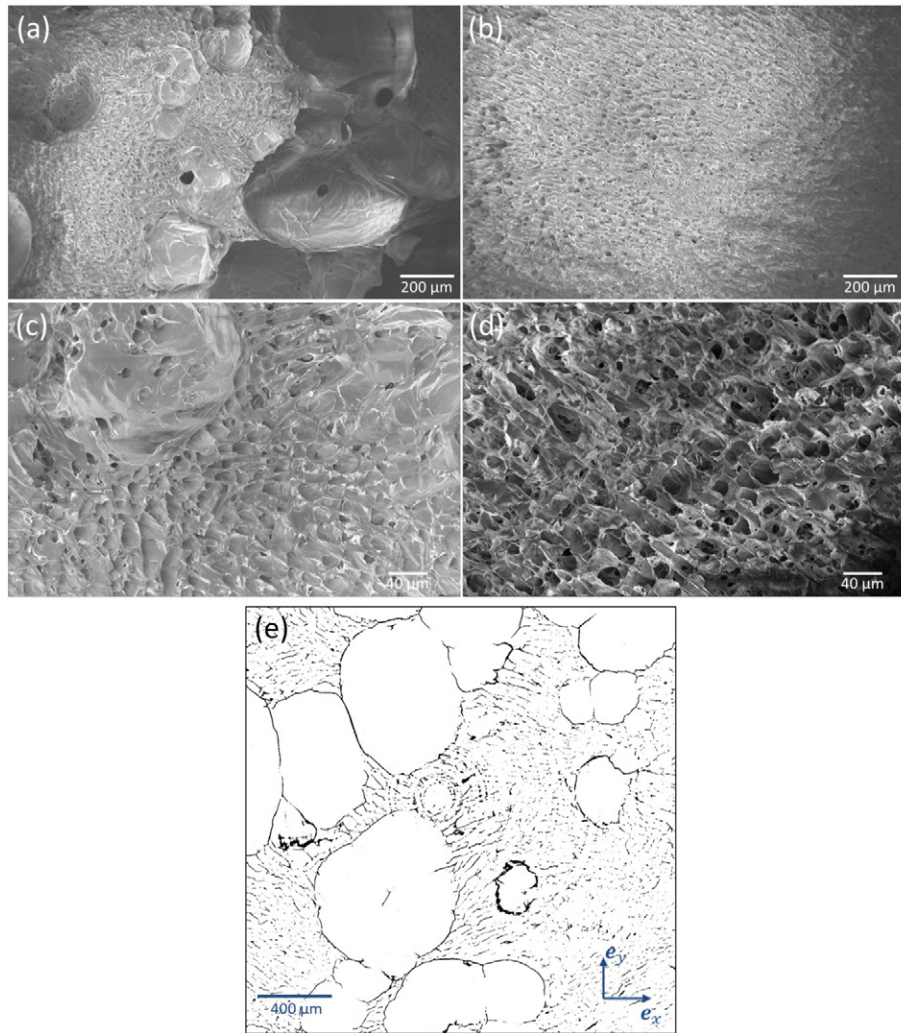**Fig. 6.** SEM micrographs showing the microstructures of various TEMPO-oxidized NFC foams ($\rho \approx 17$ kg m^{-3}, *i.e.*, $\rho/\rho_s \approx 1.2\%$) obtained using the sorbet (a,c) and quenching (b,d) processing routes. (e) Horizontal cross-section of TEMPO-oxidized NFC foam (sorbet-like process) obtained using X-ray microtomography (voxel size: 1.6^3 µm^3).

samples. Some differences were observed at higher strains: the stress-strain curve exhibited a weak strain-hardening regime instead of a pronounced increase, as shown in Fig. 7. Several potential origins could explain this discrepancy, *e.g.*, the potential degradation of the NFC structure due to the exposure to X-ray radiations and the viscoelastic effects associated with the deformation of the foam. Moreover, the compression test was interrupted to perform the scans, inducing noticeable stress relaxations, as shown in Fig. 9.

The 2D segmented micrographs shown in Fig. 9 (see also Fig. 2 in Supplementary Materials) first revealed the aforementioned auxetic effect: in the early stage of compression (*i.e.*, for $0 < \varepsilon < 0.11$), the Poisson ratio ν was estimated to be approximately -0.1 in the central zone of the sample ($h_0/10 \leq z \leq h_0 - h_0/10$). In addition, Fig. 9 shows that for $\varepsilon > 0.11$, the foam exhibited spatially heterogeneous deformation during compression (see for instance the deformation band localized in the upper part of the sample).

Fig. 10 shows high resolution 3D views (voxel size: 0.32^3 µm^3) of the microstructure of the compressed NFC foam and its evolution during compression.

3.4.3.1. First compression stop. At $\varepsilon = 0.11$, *i.e.*, just at the onset of the yield stress, most of the cells in the sample were slightly deformed (and rotated). Cell walls were primarily deformed by bending/buckling mechanisms, in particular those oriented in a direction parallel to the

compression direction: these mechanisms are highlighted in zooms around the cell labelled 1 in Fig. 10. In addition, it is worth to note that some of the cell walls were also irreversibly damaged and fractured (see the red circle in the 3D image on the top right).

3.4.3.2. Second compression stop. At $\varepsilon = 0.8$, the foam exhibited a spatially heterogeneous collapse of its cellular structure. Some of the foam cells were severely distorted. This phenomenon was associated with cell wall cracking/tearing (Fig. 10b) and the formation of plastic hinges, whereas other parts of the structure were less affected by the increase in the overall compression strain.

3.4.3.3. Third compression stop. At $\varepsilon = 2.2$, the structure was densely packed: all foam cells were collapsed. The foam cell walls began to impinge on each other, leading to a pronounced rise in the stress level (pronounced densification regime).

3.5. Effect of the processing conditions

A non-linear evolution of the apparent modulus E and yield stress σ_y with the freezing temperature is shown in Fig. 11. Regardless of the type of foam, E and σ_y were practically independent of the freezing temperature for $-114\ °C \leq T \leq -80\ °C$. In this temperature range, no pronounced changes in the cellular structure of the foams were also detected (Fig. 4 and Fig. 5). In contrast, between $-80\ °C$ and $-13\ °C$, E and
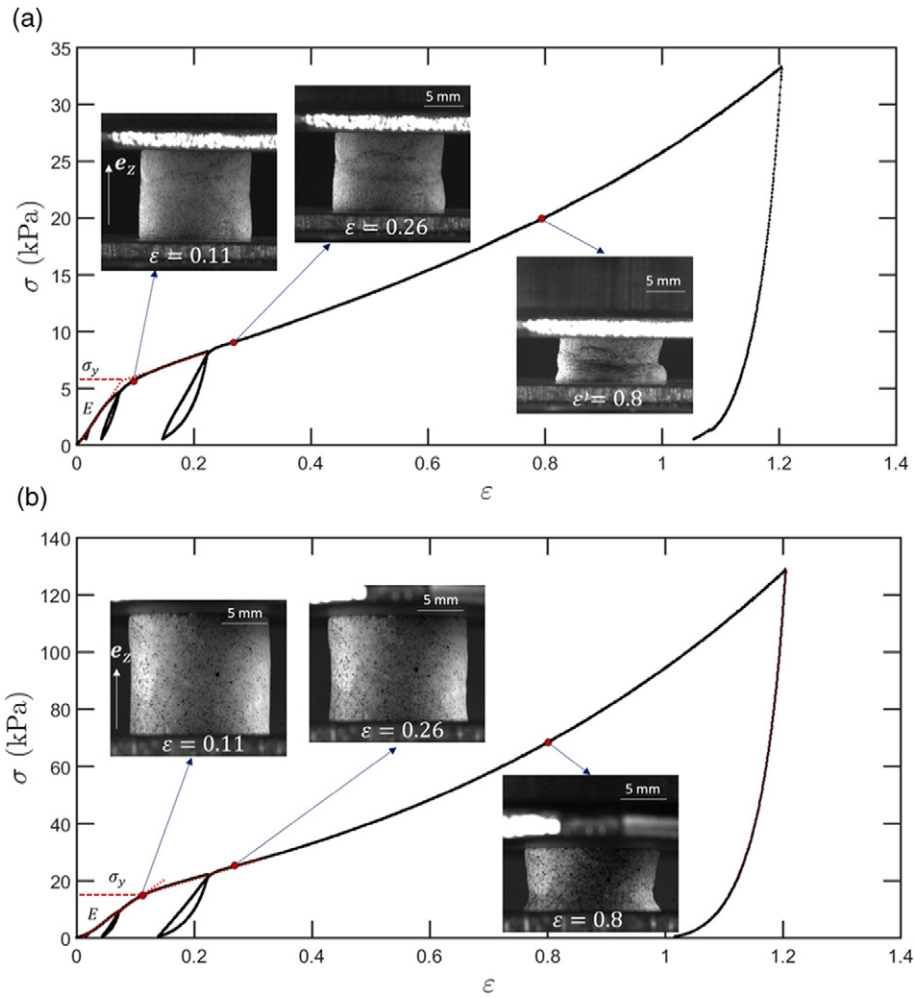
Fig. 7. Typical stress-strain curves of (a) a TEMPO-oxidized NFC foam ($\rho \approx 11$ kg m^{-3}, i.e., $\rho/\rho_s \approx 0.75$%) obtained after freezing at $T = -13$ °C and (b) an enzymatic NFC foam ($\rho \approx 23$ kg m^{-3}, i.e., $\rho/\rho_s \approx 1.7$%) obtained after freezing at $T = -68$ °C. The image insets show the evolution of the geometry of the foams during simple compression.

σ_y increased significantly with increasing the freezing temperature. In the same time, Figs. 4 and 5 show that the NFC foams exhibited pronounced microstructure variations for this temperature range, regardless of the type of NFCs.

Stress-strain curves plotted in Fig. 12 show the undeniable role of the cellular architecture of NFC foams on their mechanical response [25]. Indeed, the sorbet-like foam with a bimodal cellular structure exhibited higher mechanical performances with a modulus E and a yield
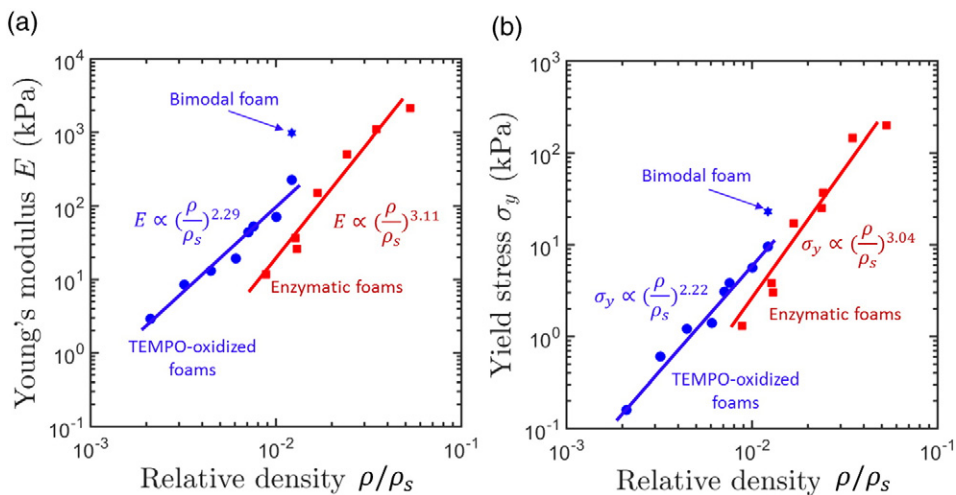

Fig. 8. Apparent compression modulus E (a) and yield stress σ_y, (b) as a function of the relative density ρ/ρ_s. Enzymatic and TEMPO NFC foams were prepared using a quenching temperature of -68 °C.
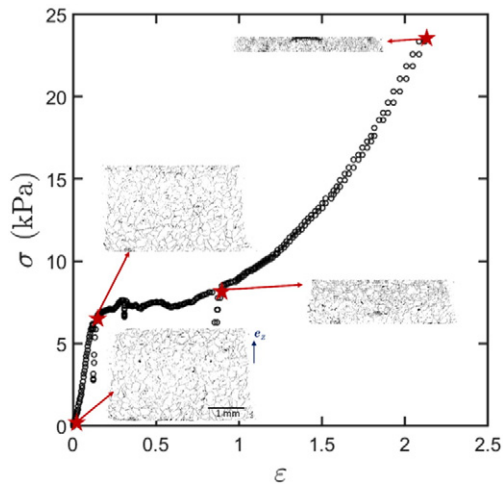
Fig. 9. Compression stress-strain curve of a TEMPO-oxidized NFC foam ($\rho \approx 11$ kg m^{-3}, $\rho/\rho_s \approx 0.75\%$, quenching temperature $T = -13$ °C) with 3D *in situ* observation of its microstructure. The insets are several cross sections along the vertical direction of 3D segmented images (voxel size: 1.6^3 μm^3), showing the evolution of the geometry of the entire foam during compression.

stress σ_y that were three to four times greater and two times greater, respectively, than those of the foams with the same relative density and prepared by quenching.

4. Discussion

The experimental results presented in the previous section clearly emphasized the leading effects of ice-templating conditions, NFC concentration and type on the microstructure of the fabricated NFC foams. These results also showed that process-induced microstructures had noticeable effects on the mechanical properties of NFC foams. The effects of freezing conditions and their influence on the microstructural and mechanical properties of NFC foams are further discussed in the following sections.

4.1. Effects of freezing conditions

Fig. 4 show that the mean radial pore size varied significantly with the applied freezing temperature. This trend, which was observed for both types of NFCs and for various NFC concentrations, could be explained by the following scenario:

- At low freezing temperature and thus high average cooling rate, nucleation rate is higher than crystal growth rate [30]. Consequently, a large number of small ice crystals are probably formed during freezing and the porous microstructure of NFC foams consists of uniform small pores (Fig. 4c).
- At higher freezing temperature and lower average cooling rate, the opposite trend could take place. Ice crystal growth is more kinetically favored than ice nucleation [30]. Thus, a small number of large ice crystals are probably formed during freezing. This phenomenon is potentially at the origin of the formation of large pores after ice sublimation.

These results indicate that the control of crystal nucleation and growth prior to freeze-drying is crucial in "building" the microstructure of NFC foams. Adapting the quenching temperature could be used to control the foam pore size (Fig. 4).

However, Fig. 4 also shows that direct quenching did not enable the shape and the orientation of ice crystals to be properly controlled. Indeed, using this freezing procedure, temperature gradients in the frozen

samples were not controlled and exhibited preferred directions. The ice crystal growth was columnar and the resulting foams had highly anisotropic pore structures. Thus, to obtain isotropic pores, we proposed an alternate freezing procedure that consisted in using a mechanical stirring of the solidifying suspensions at constant freezing temperature. Fig. 6 clearly shows that the pores induced during mechanical stirring at a high freezing temperature were large and rounded: they were mechanically eroded and constrained to grow isotropically. The subsequent quenching with a high cooling rate induced a second population of finer and anisotropic ice crystals.

Thus, with these preliminary results it was demonstrated that combining several sequences of quenching and mechanical stirring was efficient to obtain foam microstructures with controlled pore size, population and anisotropy.

4.2. Effects of NFC type

Figs. 4 and 5 also clearly show the noticeable structural differences between enzymatic and TEMPO-oxidized NFC foams. This illustrates the undeniable role of the NFC nanostructures and physico-chemical properties on the phenomena of particle segregation, entrapment and redistribution that occur during ice growth [30]. Because of their smallest dimensions, highest aspect ratio, and strongest colloidal stability (Section 2.1), TEMPO-oxidized NFCs are presumably more homogenously redistributed by the moving ice front, leading to more regular structures. The situation is probably more complex and chaotic with enzymatic suspensions since they are more polydisperse, less stable and thus exhibit mesoscale heterogeneities in the form of NFC flocs or floc chains (Fig. 2a, c, floc size $\approx$ 50–100 μm) [42]. These flocs could be encapsulated or torn by the moving ice front [28–30], instead of being homogeneously redistributed. These complex mechanisms are potentially at the origin of the structural defects and heterogeneities, such as the numerous dangling masses and torn cell walls, as shown in Fig. 5.

4.3. Effects of NFC concentration

The macroscopic shrinkage of the NFC foams observed in Fig. 3 could be potentially attributed to several combined microscale mechanisms:

- During solidification, NFC depletion or migration could take place. This type of phenomenon is known to preferentially occur in weakly stabilized colloidal systems such as flocculated and dilute colloidal suspensions, and for low freezing rates [28–30].
- During drying, i.e., during sublimation of ice-crystals, folding of the cells could result from the release of internal stresses that were induced in the cell walls during the nucleation and growth of ice crystals.
- During drying, folding and shrinkage of cell walls could also be induced by the hygroexpansion-related shrinkage of NFCs.

The NFC concentration in the suspensions presumably plays a major role in the aforementioned mechanisms. Indeed, as shown in Fig. 3, the foam shrinkage exhibited a drastic increase below a critical NFC concentration c^* below which the entangled NFC networks lost their mechanical integrity. This critical concentration could also correspond to a critical number of bonds [57–60] or interactions per nanofiber z^*. Below this critical coordination number z^*, NFC depletion or migration phenomena that are induced by ice formation could be facilitated, in particular near the sample external surface. The mean coordination number z of fibrous networks of homogeneously distributed straight fibers can be estimated using the statistical tube model [52,61–62]:

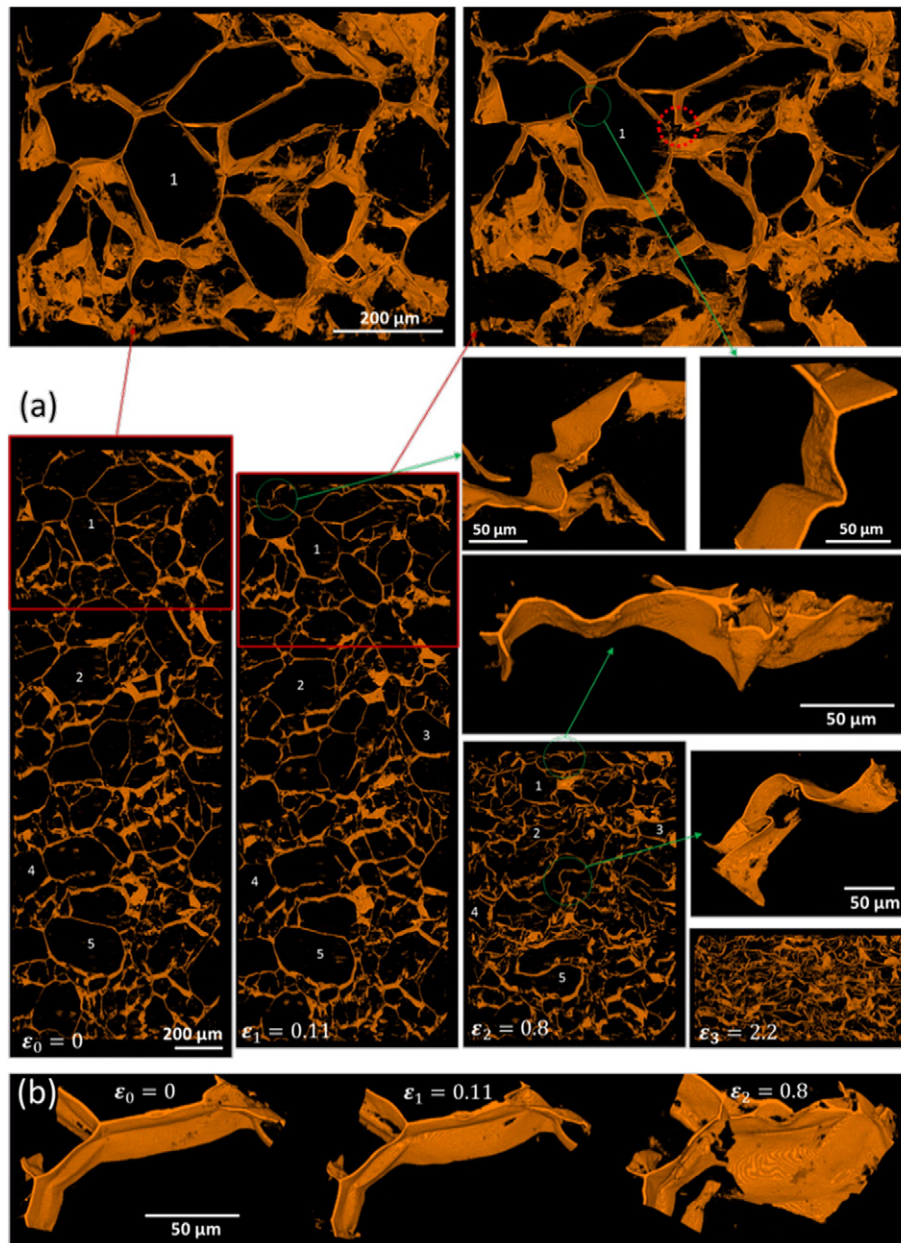$$z = 4\phi\left(\frac{2}{\pi}r\Phi_1 + \Phi_2 + 1\right), \tag{1}$$

Fig. 10. (a) 3D images (voxel size: 0.32^3 µm^3, volume size $\approx 818 \times 818 \times 12$ µm^3) of the internal microstructure of a TEMPO-oxidized NFC foam ($\rho \approx 10$ kg m^{-3}, quenching temperature $T = -13$ °C) and its evolution during compression. The insets show zooms on several regions of the foam. (b) 3D images of a junction between several foam cells and its deformation and fracture during compression. Note that some cells that are numbered from 1 to 5 to help the reader to visualize the evolution of the geometry of typical foam cells under compression.

where $r = l/d$ is the aspect ratio of the fibers and Φ_1, Φ_2 the orientation distribution functions ($\Phi_1 = \pi 4$ and $\Phi_2 = 1/2$ for 3D random fibrous networks). Hence, using this approximate and considering that $r = 100$ and 300 for enzymatic [42,58] and TEMPO-oxidized NFCs [52], respectively, the mean coordination number z of networks with 3D random nanofiber orientations was estimated, at a first order, as a function of the NFC volume fraction ϕ. Fig. 13 shows the evolution of the diameter reduction measured for enzymatic and TEMPO-oxidized foams (Fig. 3) as a function of the mean coordination number z. For both types of NFC suspensions, the macroscopic foam diameter suddenly decreased below a critical coordination number $z^* \approx 1 - 2$. Note that this value is close to those predicted from the percolation theory for networks of slender fibers [52,63–65]. The slight difference between TEMPO-oxidized NFC and enzymatic NFC suspensions could result

from differences in the electrostatic charge of NFCs [52,59–60]. Note that this estimate should be considered as a first approximation for the enzymatic suspensions since they exhibited flocculated textures [42].

Above the critical concentration c^*, the role of the NFC concentration is also important. As reported by Sehaqui et al. [11] for enzymatic NFC foams, increasing the NFC concentration c yields a decrease in the foam pore size. A similar effect was obtained for the studied enzymatic foams (Fig. 5), but also for TEMPO-oxidized foams (Fig. 4). The decrease in the foam pore size could be correlated to the increase, with c (or ϕ, or z see Eq. (1)), in the rheological properties of the suspensions, namely the yield stress [52,66]. Higher yield stress would restrain ice crystal growth so that more nucleation sites would be induced, resulting in the formation of numerous small pores.
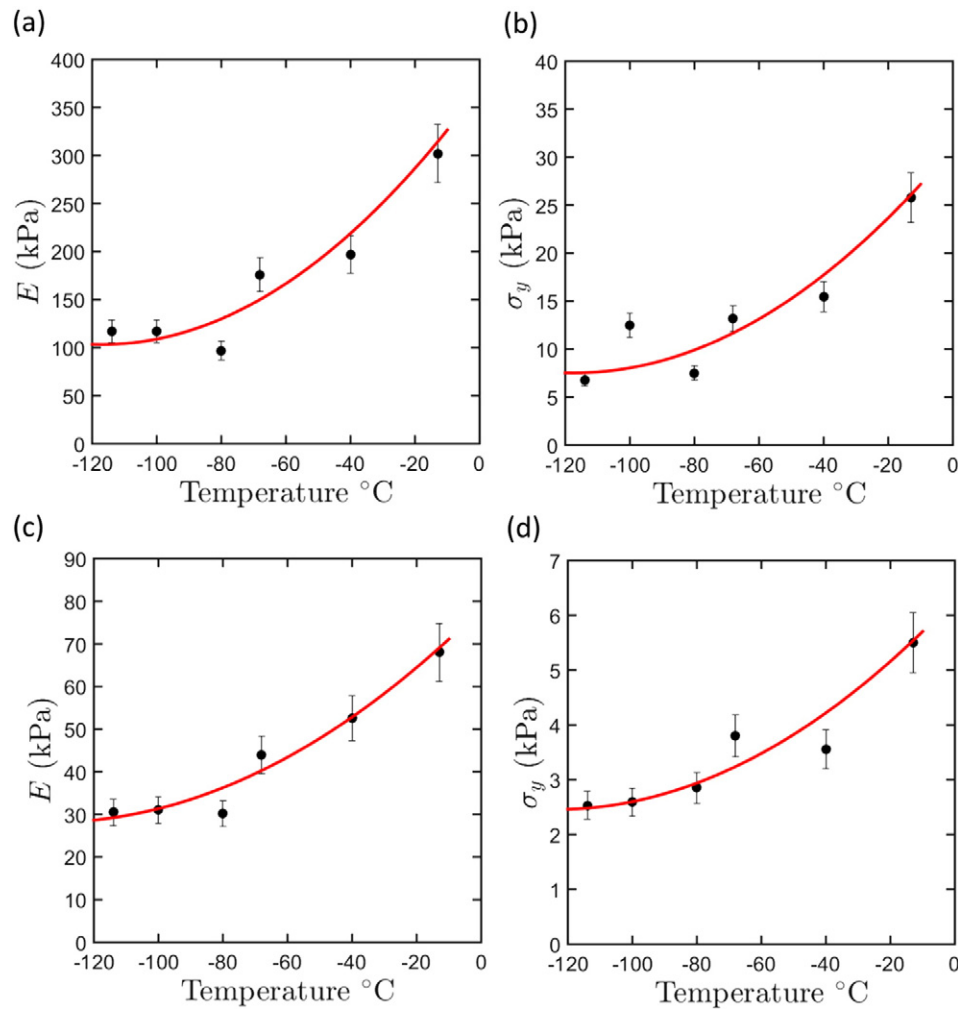
Fig. 11. Apparent compression modulus E and yield stress σ_y as a function of the freezing temperature for (a,b) enzymatic NFC foams ($\rho \approx 23$ kg m^{-3}, $\rho/\rho_s \approx 1.7\%$) and (c,d) TEMPO-oxidized NFC foams ($\rho \approx 11$ kg m^{-3}, $\rho/\rho_s \approx 0.75\%$).

4.4. Potential origins of the particular mechanical properties of NFC foams

4.4.1. Potential origins of scaling laws

The scaling exponents ($n = 2.29$ and $m = 2.22$) of TEMPO-oxidized foams were close to those expected for classical cellular materials [25–26,67] with well-defined microstructures and deformation mechanisms, such as open ($n = 2$ and $m = 1.5$) or closed foams without thickening of edges ($n = 3$ and $m = 2$). These exponents are consistent with deformation micro-mechanisms that are governed both by plate and strut bending. This assumption is in accordance with the microtomographic images (Fig. 10) that show bending and buckling of both ridges and thin walls of cells. However, note that the slightly higher values could be attributed to the role played by the remaining partially fibrillated fibers (Fig. 2).

In contrast, the scaling exponents ($n = 3.11$ and $m = 3.04$) of enzymatic NFC foams were close to those usually obtained for aerogels [68–73], i.e., $3 < n < 4$ and $2.5 < m < 3.5$. This behavior could be directly related to the disordered cellular structure of these foams and more precisely to the existence of numerous dangling masses or branches that hung off the cell walls [72–73] (Fig. 5). These portions of cells could act as "dead zones" that did not bear the applied load. Their volume fraction was difficult to determine using the 2D and 3D micrographs which are shown in Fig. 5. However, the amount of these "dead zones" is expected to decrease as the NFC content increases, which could progressively induce an evolution of the nature of the mechanical behavior of enzymatic foams.

Lastly, Fig. 8 also shows the importance of controlling the internal microstructures of NFC foams. TEMPO-oxidized NFC foams had a less erratic cellular architecture than that of enzymatic NFC foams, resulting in higher specific mechanical properties and lower scaling exponents. Additionally, obtaining bimodal foam pore structures also enhanced the specific mechanical properties, as shown in Fig. 8.

4.4.2. Potential origins of the strain hardening and the auxetic behavior of NFC foams

The strain hardening behavior of TEMPO-oxidized and enzymatic NFC foams was different from that usually observed for elasto-viscoplastic foams for which the strain hardening is much weaker. This strain hardening, which can be very interesting for structural applications, is rather close to that observed for crumpled sheets, self-locked materials and entangled fibrous media [67,74]. It is worth to note that TEMPO-oxidized NFC foams (Fig. 4e) exhibited several structural similarities with crumpled aluminum or paper thin foils [67,75–79].

In accordance with the tomographic images shown in Fig. 10, the strain-hardening behavior of NFC foams could result from a progressive and spatially heterogeneous load-induced collapse/crushing mechanism (local densification). In addition, the crushing is often induced by the high bending/buckling of cell walls, leading to re-entrant deformation micro-mechanisms that could presumably be at the origin of the auxetic behavior observed at the mesoscale (Fig. 7). Similar re-entrant mechanisms have already been reported for auxetic materials such as polymer foams [80] and crumpled foils [67].
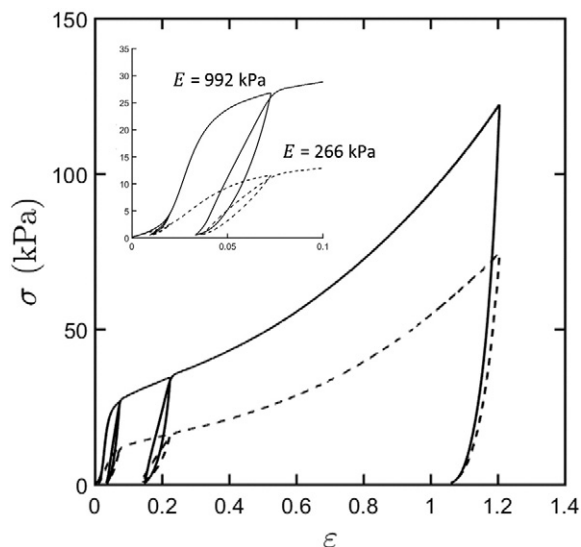
Fig. 12. Stress-strain curves of TEMPO-oxidized NFC foams ($\rho \approx 17$ kg m^{-3}, $\rho/\rho_s \approx 1.2\%$) fabricated using both the quenching (freezing temperature $T = -68°C$, dashed line) and sorbet (solid line) processing routes. The inset shows a zoom on the early stage of the curves.

5. Conclusion

This study showed that the colloidal properties and homogeneity of NFC aqueous suspensions greatly affected the NFC foam cell structures and their mechanical properties. Foams prepared using stabilized NFC suspensions with narrow particle size polydispersity, such as TEMPO-oxidized NFC suspensions exhibited more regular cellular architectures and higher specific mechanical properties. This study also revealed that NFC concentration as well as NFC morphology played a major role on the foam shrinkage and the geometry of foam cells. The foam diameter shrinkage strain suddenly increased below a critical NFC concentration c^* that depended on the NFC aspect ratio r. Using volume excluded concepts, it was demonstrated that this critical concentration c^* probably corresponded to be a percolation threshold below which NFC networks were no longer connected and lost their mechanical integrity.
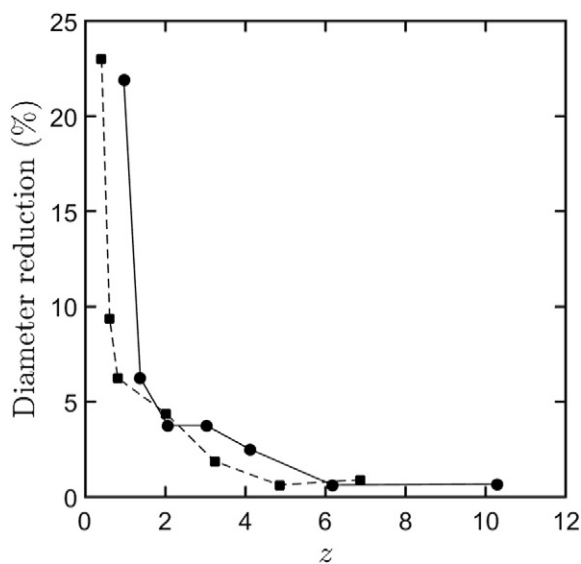
In addition, it was shown that the control of crystal nucleation and their growth prior to freeze-drying was crucial in building the cellular architecture of NFC foams. Changing the quenching temperature was an easy way to control the foam pore size. However, this technique did not enable the shape and orientation of crystals to be properly modified. To circumvent this problem, an original alternate freezing procedure that consisted of using during freezing a mechanical stirring of the solidifying suspensions was proposed. This strategy enabled NFC foams with interesting bimodal cell structures and enhanced mechanical properties to be obtained. This preliminary work revealed that combining several sequences of quenching and mechanical stirring was efficient for obtaining foam microstructures with tailored pore size, population and anisotropy. However, further investigations are required to optimize the process-induced microstructures of the foams prepared using this technique. For instance, it could be of great importance to assess the effect of the stirring velocity, time as well as quenching temperature on the microstructure and mechanics.

Finally, this study showed that synchrotron X-ray microtomography was a suitable and efficient tool to enhance the description of the complex microstructure of NFC foams and to unveil the role of deformation mechanisms at the cell scale on their mechanical response. Using this technique, several mesoscale deformation mechanisms that could be at the origin of the macroscale auxetic and strain-hardening behaviors of NFC foams were identified.

Acknowledgements

Appendix A. Supplementary data

Supplementary data to this article can be found online at http://dx.doi.org/10.1016/j.matdes.2016.04.088.

Fig. 13. Diameter reduction of NFC foams (data shown in Fig. 3) as a function of the mean coordination number z for enzymatic NFCs (black circle symbols) and TEMPO-oxidized NFCs (black square symbols).

References

[1] L.J. Gibson, The hierarchical structure and mechanics of plant materials, J. R. Soc. Interface 9 (2012) 2749–2766, http://dx.doi.org/10.1098/rsif.2012.0341.
[2] D. Klemm, B. Heublein, H.-P. Fink, A. Bohn, Cellulose: fascinating biopolymer and sustainable raw material, Angew. Chem. Int. Ed. 44 (2005) 3358–3393.
[3] J.-L. Wertz, J.P. Mercier, O. Bédué, Cellulose Science and Technology, CRC Press, 2010.
[4] K. Abe, S. Iwamoto, H. Yano, Obtaining cellulose nanofibers with a uniform width of 15 nm from wood, Biomacromolecules 8 (2007) 3276–3278, http://dx.doi.org/10.1021/bm700624p.
[5] H.P.S. Abdul Khalil, Y. Davoudpour, M.N. Islam, A. Mustapha, K. Sudesh, R. Dungani, et al., Production and modification of nanofibrillated cellulose using various mechanical processes: a review, Carbohydr. Polym. 99 (2014) 649–665, http://dx.doi.org/10.1016/j.carbpol.2013.08.069.
[6] M. Henriksson, G. Henriksson, L.A. Berglund, T. Lindström, An environmentally friendly method for enzyme-assisted preparation of microfibrillated cellulose (MFC) nanofibers, Eur. Polym. J. 43 (2007) 3434–3441, http://dx.doi.org/10.1016/j.eurpolymj.2007.05.038.
[7] M. Pääkkö, M. Ankerfors, H. Kosonen, A. Nykänen, S. Ahola, M. Österberg, et al., Enzymatic hydrolysis combined with mechanical shearing and high-pressure homogenization for nanoscale cellulose fibrils and strong gels, Biomacromolecules 8 (2007) 1934–1941, http://dx.doi.org/10.1021/bm061215p.
[8] T. Saito, S. Kimura, Y. Nishiyama, A. Isogai, Cellulose nanofibers prepared by TEMPO-mediated oxidation of native cellulose, Biomacromolecules 8 (2007) 2485–2491, http://dx.doi.org/10.1021/bm0703970.
[9] A. Isogai, T. Saito, H. Fukuzumi, TEMPO-oxidized cellulose nanofibers, Nanoscale 3 (2011) 71–85, http://dx.doi.org/10.1039/C0NR00583E.

[10] T. Saito, T. Uematsu, S. Kimura, T. Enomae, A. Isogai, Self-aligned integration of native cellulose nanofibrils towards producing diverse bulk materials, Soft Matter 7 (2011) 8804–8809, http://dx.doi.org/10.1039/C1SM06050C.

[11] H. Sehaqui, M. Salajková, Q. Zhou, L.A. Berglund, Mechanical performance tailoring of tough ultra-high porosity foams prepared from cellulose I nanofiber suspensions, Soft Matter 6 (2010) 1824–1832, http://dx.doi.org/10.1039/B927505C.

[12] Z.M. Ali, L.J. Gibson, The structure and mechanics of nanofibrillar cellulose foams, Soft Matter 9 (2013) 1580–1588, http://dx.doi.org/10.1039/C2SM27197D.

[13] A.E. Donius, A. Liu, L.A. Berglund, U.G.K. Wegst, Superior mechanical performance of highly porous, anisotropic nanocellulose–montmorillonite aerogels prepared by freeze casting, J. Mech. Behav. Biomed. Mater. 37 (2014) 88–99, http://dx.doi.org/10.1016/j.jmbbm.2014.05.012.

[14] J. Lee, Y. Deng, The morphology and mechanical properties of layer structured cellulose microfibril foams from ice-templating methods, Soft Matter 7 (2011) 6034–6040, http://dx.doi.org/10.1039/C1SM05388D.

[15] H. Sehaqui, Q. Zhou, L.A. Berglund, High-porosity aerogels of high specific surface area prepared from nanofibrillated cellulose (NFC), Compos. Sci. Technol. 71 (2011) 1593–1599, http://dx.doi.org/10.1016/j.compscitech.2011.07.003.

[16] Y. Kobayashi, T. Saito, A. Isogai, Aerogels with 3D ordered nanofiber skeletons of liquid-crystalline nanocellulose derivatives as tough and transparent insulators, Angew. Chem. 126 (2014) 10562–10565, http://dx.doi.org/10.1002/ange.201405123.

[17] A.J. Benítez, J. Torres-Rendon, M. Poutanen, A. Walther, Humidity and multiscale structure govern mechanical properties and deformation modes in films of native cellulose nanofibrils, Biomacromolecules 14 (2013) 4497–4506, http://dx.doi.org/10.1021/bm401451m.

[18] B. Wicklein, A. Kocjan, G. Salazar-Alvarez, F. Carosio, G. Camino, M. Antonietti, et al., Thermally insulating and fire-retardant lightweight anisotropic foams based on nanocellulose and graphene oxide, Nat. Nanotechnol. 10 (2015) 277–283.

[19] D. Bendahou, A. Bendahou, B. Seantier, Y. Grohens, H. Kaddami, Nano-fibrillated cellulose-zeolites based new hybrid composites aerogels with super thermal insulating properties, Ind. Crop. Prod. 65 (2015) 374–382, http://dx.doi.org/10.1016/j.indcrop.2014.11.012.

[20] B. Seantier, D. Bendahou, A. Bendahou, Y. Grohens, H. Kaddami, Multi-scale cellulose based new bio-aerogel composites with thermal super-insulating and tunable mechanical properties, Carbohydr. Polym. 138 (2016) 335–348, http://dx.doi.org/10.1016/j.carbpol.2015.11.032.

[21] J.T. Korhonen, M. Kettunen, R.H.A. Ras, O. Ikkala, Hydrophobic nanocellulose aerogels as floating, sustainable, reusable, and recyclable oil absorbents, ACS Appl. Mater. Interfaces 3 (2011) 1813–1816, http://dx.doi.org/10.1021/am200475b.

[22] N.T. Cervin, C. Aulin, P.T. Larsson, L. Wågberg, Ultra porous nanocellulose aerogels as separation medium for mixtures of oil/water liquids, Cellulose 19 (2011) 401–410, http://dx.doi.org/10.1007/s10570-011-9629-5.

[23] Z. Zhang, G. Sèbe, D. Rentsch, T. Zimmermann, P. Tingaut, Ultralightweight and flexible silylated nanocellulose sponges for the selective removal of oil from water, Chem. Mater. 26 (2014) 2659–2668, http://dx.doi.org/10.1021/cm5004164.

[24] H. Cai, S. Sharma, W. Liu, W. Mu, W. Liu, X. Zhang, et al., Aerogel microspheres from natural cellulose nanofibrils and their application as cell culture scaffold, Biomacromolecules 15 (2014) 2540–2547, http://dx.doi.org/10.1021/bm5003976.

[25] L.J. Gibson, M.F, Structure and Properties, Cambridge University Press, Ashby, Cellular Solids, 1997.

[26] N. Mills, Polymer Foams Handbook: Engineering and Biomechanics Applications and Design Guide, Butterworth-Heinemann, 2007.

[27] N.T. Cervin, L. Andersson, J.B.S. Ng, P. Olin, L. Bergström, L. Wågberg, Lightweight and strong cellulose materials made from aqueous foams stabilized by nanofibrillated cellulose, Biomacromolecules 14 (2013) 503–511, http://dx.doi.org/10.1021/bm301755u.

[28] S. Deville, Freeze-casting of porous biomaterials: structure, properties and opportunities, Materials 3 (2010) 1913–1927, http://dx.doi.org/10.3390/ma3031913.

[29] S. Deville, Ice-templating, freeze casting: beyond materials processing, J. Mater. Res. 28 (2013) 2202–2219, http://dx.doi.org/10.1557/jmr.2013.105.

[30] W.L. Li, K. Lu, J.Y. Walz, Freeze casting of porous materials: review of critical factors in microstructure evolution, Int. Mater. Rev. 57 (2012) 37–60, http://dx.doi.org/10.1179/1743280411Y.0000000011.

[31] S. Deville, E. Maire, G. Bernard-Granger, A. Lasalle, A. Bogner, C. Gauthier, et al., Metastable and unstable cellular solidification of colloidal suspensions, Nat. Mater. 8 (2009) 966–972.

[32] F.J. O'Brien, B.A. Harley, I.V. Yannas, L. Gibson, Influence of freezing rate on pore structure in freeze-dried collagen-GAG scaffolds, Biomaterials 25 (2004) 1077–1086, http://dx.doi.org/10.1016/S0142-9612(03)00630-6.

[33] A.J. Svagan, M.A.S.A. Samir, L.A. Berglund, Biomimetic foams of high mechanical performance based on nanostructured cell walls reinforced by native cellulose nanofibrils, Adv. Mater. 20 (2008) 1263–1269, http://dx.doi.org/10.1002/adma.200701215.

[34] C. Aulin, J. Netrval, L. Wågberg, T. Lindström, Aerogels from nanofibrillated cellulose with tunable oleophobicity, Soft Matter 6 (2010) 3298–3305, http://dx.doi.org/10.1039/C001939A.

[35] T.C.F. Silva, Y. Habibi, J.L. Colodette, T. Elder, L.A. Lucia, A fundamental investigation of the microarchitecture and mechanical properties of tempo-oxidized nanofibrillated cellulose (NFC)-based aerogels, Cellulose 19 (2012) 1945–1956, http://dx.doi.org/10.1007/s10570-012-9761-x.

[36] J. Lin, L. Yu, F. Tian, N. Zhao, X. Li, F. Bian, et al., Cellulose nanofibrils aerogels generated from jute fibers, Carbohydr. Polym. 109 (2014) 35–43, http://dx.doi.org/10.1016/j.carbpol.2014.03.045.

[37] W. Chen, H. Yu, Q. Li, Y. Liu, J. Li, Ultralight and highly flexible aerogels with long cellulose I nanofibers, Soft Matter 7 (2011) 10360–10368, http://dx.doi.org/10.1039/C1SM06179H.

[38] L. Melone, L. Altomare, I. Alfieri, A. Lorenzi, L. De Nardo, C. Punta, Ceramic aerogels from TEMPO-oxidized cellulose nanofibre templates: synthesis, characterization, and photocatalytic properties, J. Photochem. Photobiol. Chem. 261 (2013) 53–60, http://dx.doi.org/10.1016/j.jphotochem.2013.04.004.

[39] P. Munier, K. Gordeyeva, L. Bergström, A.B. Fall, Directional freezing of nanocellulose dispersions aligns the rod-like particles and produces low-density and robust particle networks, Biomacromolecules (2016) http://dx.doi.org/10.1021/acs.biomac.6b00304 (accessed April 16, 2016).

[40] M. Sedighi Gilani, M.N. Boone, J.L. Fife, S. Zhao, M.M. Koebel, T. Zimmermann, P. Tingaut, Structure of cellulose -silica hybrid aerogel at sub-micron scale, studied by synchrotron X-ray tomographic microscopy, Compos. Sci. Technol. 124 (2016) 71–80, http://dx.doi.org/10.1016/j.compscitech.2016.01.013.

[41] C. Zhang, B. Zhu, D. Li, L.J. Lee, Extruded polystyrene foams with bimodal cell morphology, Polymer 53 (2012) 2435–2442, http://dx.doi.org/10.1016/j.polymer.2012.04.006.

[42] F. Martoïa, C. Perge, P.J.J. Dumont, L. Orgéas, M.A. Fardin, S. Manneville, M.N. Belgacem, Heterogeneous flow kinematics of cellulose nanofibril suspensions under shear, Soft Matter 11 (2015) 4742–4755, http://dx.doi.org/10.1039/C5SM00530B.

[43] L. Salmén, C. Fellers, The nature of volume hydroexpansivity of paper, J. Pulp Pap. Sci. 15 (1989) J63–J65.

[44] D. Brabazon, D.J. Browne, A.J. Carr, Mechanical stir casting of aluminium alloys from the mushy state: process, microstructure and mechanical properties, Mater. Sci. Eng. A 326 (2002) 370–381, http://dx.doi.org/10.1016/S0921-5093(01)01832-9.

[45] D.H. Kirkwood, Semisolid metal processing, Int. Mater. Rev. 39 (1994) 173–189, http://dx.doi.org/10.1179/imr.1994.39.5.173.

[46] L. Salvo, P. Cloetens, E. Maire, S. Zabler, J.J. Blandin, J.Y. Buffière, et al., X-ray microtomography an attractive characterisation technique in materials science, Nucl. Instrum. Methods Phys. Res., Sect. B 200 (2003) 273–286, http://dx.doi.org/10.1016/S0168-583X(02)01689-0.

[47] P. Cloetens, W. Ludwig, J. Baruchel, J.-P. Guigay, P. Pernot-Rejmánková, Murielle Salomé-Pateyron, et al., hard X-ray phase imaging using simple propagation of a coherent synchrotron radiation beam, J. Phys. Appl. Phys. 32 (1999) A145, http://dx.doi.org/10.1088/0022-3727/32/10A/330.

[48] M.A. Beltran, D.M. Paganin, K. Uesugi, M.J. Kitchen, 2D and 3D X-ray phase retrieval of multi-material objects using a single defocus distance, Opt. Express 18 (2010) 6423, http://dx.doi.org/10.1364/OE.18.006423.

[49] D. Paganin, S.C. Mayo, T.E. Gureyev, P.R. Miller, S.W. Wilkins, Simultaneous phase and amplitude extraction from a single defocused image of a homogeneous object, J. Microsc. 206 (2002) 33–40, http://dx.doi.org/10.1046/j.1365-2818.2002.01010.x.

[50] P. Latil, L. Orgéas, C. Geindreau, P.J.J. Dumont, S. Rolland, du Roscoat, Towards the 3D in situ characterisation of deformation micro-mechanisms within a compressed bundle of fibres, Compos. Sci. Technol. 71 (2011) 480–488, http://dx.doi.org/10.1016/j.compscitech.2010.12.023.

[51] A. Isogai, Wood nanocelluloses: fundamentals and applications as new bio-based nanomaterials, J. Wood Sci. 59 (2013) 449–459, http://dx.doi.org/10.1007/s10086-013-1365-z.

[52] F. Martoïa, P.J.J. Dumont, L. Orgéas, M.N. Belgacem, J.-L. Putaux, Micro-mechanics of electrostatically stabilized suspensions of cellulose nanofibrils under steady state shear flow, Soft Matter 12 (2016) 1721–1735, http://dx.doi.org/10.1039/C5SM02310F.

[53] I. Usov, G. Nyström, J. Adamcik, S. Handschin, C. Schütz, A. Fall, et al., Understanding nanocellulose chirality and structure-properties relationship at the single fibril level, Nat. Commun. 6 (2015) 7564, http://dx.doi.org/10.1038/ncomms8564.

[54] Y. Su, C. Burger, H. Ma, B. Chu, B.S. Hsiao, Morphological and property investigations of carboxylated cellulose nanofibers extracted from different biological species, Cellulose 22 (2015) 3127–3135, http://dx.doi.org/10.1007/s10570-015-0698-8.

[55] F. Jiang, Y.-L. Hsieh, Super water absorbing and shape memory nanocellulose aerogels from TEMPO-oxidized cellulose nanofibrils via cyclic freezing–thawing, J. Mater. Chem. A 2 (2013) 350–359, http://dx.doi.org/10.1039/C3TA13629A.

[56] D. Rodney, B. Gadot, O.R. Martinez, S. Rolland du Roscoat, L. Orgéas, Reversible dilatancy in entangled single-wire materials, Nat. Mater. 15 (2016) 72–77, http://dx.doi.org/10.1038/nmat4429.

[57] W.W. Sampson, Modelling Stochastic Fibrous Materials With Mathematica®, Springer Science & Business Media, 2008.

[58] S. Varanasi, R. He, W. Batchelor, Estimation of cellulose nanofibre aspect ratio from measurements of fibre suspension gel point, Cellulose 20 (2013) 1885–1896, http://dx.doi.org/10.1007/s10570-013-9972-9.

[59] A. Wierenga, A.P. Philipse, H.N.W. Lekkerkerker, D.V. Boger, Aqueous dispersions of colloidal boehmite: structure, dynamics, and yield stress of rod gels, Langmuir 14 (1998) 55–65, http://dx.doi.org/10.1021/la970376z.

[60] S.R. Raghavan, J.F. Douglas, The conundrum of gel formation by molecular nanofibers, wormlike micelles, and filamentous proteins: gelation without cross-links? Soft Matter 8 (2012) 8539–8546, http://dx.doi.org/10.1039/C2SM25107H.

[61] S. Toll, Note: on the tube model for fiber suspensions, J. Rheol. 37 (1993) 123–125, http://dx.doi.org/10.1122/1.550460.

[62] L. Orgéas, P.J.J. Dumont, J.-P. Vassal, O. Guiraud, V. Michaud, D. Favier, In-plane conduction of polymer composite plates reinforced with architectured networks of copper fibres, J. Mater. Sci. 47 (2012) 2932–2942, http://dx.doi.org/10.1007/s10853-011-6126-z.

[63] L. Berhan, A.M. Sastry, Modeling percolation in high-aspect-ratio fiber systems. II. The effect of waviness on the percolation onset, Phys. Rev. E 75 (2007) 041121, http://dx.doi.org/10.1103/PhysRevE.75.041121.

[64] A.P. Philipse, The random contact equation and its implications for (colloidal) rods in packings, suspensions, and anisotropic powders, Langmuir 12 (1996) 1127–1133, http://dx.doi.org/10.1021/la950671o.

[65] R.J. Hill, Elastic modulus of Microfibrillar cellulose gels, Biomacromolecules 9 (2008) 2963–2966, http://dx.doi.org/10.1021/bm800490x.

[66] M. Mohtaschemi, K. Dimic-Misic, A. Puisto, M. Korhonen, T. Maloney, J. Paltakari, et al., Rheological characterization of fibrillated cellulose suspensions via bucket vane viscometer, Cellulose 21 (2014) 1305–1312, http://dx.doi.org/10.1007/s10570-014-0235-1.

[67] O. Bouaziz, J.P. Masse, S. Allain, L. Orgéas, P. Latil, Compression of crumpled aluminum thin foils and comparison with other cellular materials, Mater. Sci. Eng. A 570 (2013) 1–7, http://dx.doi.org/10.1016/j.msea.2013.01.031.

[68] R. Sescousse, R. Gavillon, T. Budtova, Aerocellulose from cellulose–ionic liquid solutions: preparation, properties and comparison with cellulose–NaOH and cellulose–NMMO routes, Carbohydr. Polym. 83 (2011) 1766–1774, http://dx.doi.org/10.1016/j.carbpol.2010.10.043.

[69] K. Ganesan, A. Dennstedt, A. Barowski, L. Ratke, Design of aerogels, cryogels and xerogels of cellulose with hierarchical porous structures, Mater. Des. 92 (2016) 345–355, http://dx.doi.org/10.1016/j.matdes.2015.12.041.

[70] T. Woignier, J. Phalippou, R. Vacher, Parameters affecting elastic properties of silica aerogels, J. Mater. Res. 4 (1989) 688–692, http://dx.doi.org/10.1557/JMR.1989.0688.

[71] T. Woignier, J. Reynes, A. Hafidi Alaoui, I. Beurroies, J. Phalippou, Different kinds of structure in aerogels: relationships with the mechanical properties1, J. Non-Cryst. Solids 241 (1998) 45–52, http://dx.doi.org/10.1016/S0022-3093(98)00747-9.

[72] H.-S. Ma, A.P. Roberts, J.-H. Prévost, R. Jullien, G.W. Scherer, Mechanical structure–property relationship of aerogels, J. Non-Cryst. Solids 277 (2000) 127–141, http://dx.doi.org/10.1016/S0022-3093(00)00288-X.

[73] N. Hüsing, U. Schubert, Aerogels—airy materials: chemistry, structure, and properties, Angew. Chem. Int. Ed. 37 (1998) 22–45, http://dx.doi.org/10.1002/(SICI)1521-3773(19980202)37:1/2<22::AID-ANIE22>3.0.CO;2-I.

[74] R.C. Picu, Mechanics of random fiber networks—a review, Soft Matter 7 (2011) 6768–6785, http://dx.doi.org/10.1039/C1SM05022B.

[75] Y.-C. Lin, J.-M. Sun, H.W. Yang, Y. Hwu, C.L. Wang, T.-M. Hong, X-ray tomography of a crumpled plastoelastic thin sheet, Phys. Rev. E 80 (2009) 066114, http://dx.doi.org/10.1103/PhysRevE.80.066114.

[76] A.D. Cambou, N. Menon, Three-dimensional structure of a sheet crumpled into a ball, Proc. Natl. Acad. Sci. 108 (2011) 14741–14745, http://dx.doi.org/10.1073/pnas.1019192108.

[77] S. Cottrino, P. Viviès, D. Fabrègue, E. Maire, Mechanical properties of crumpled aluminum foils, Acta Mater. 81 (2014) 98–110, http://dx.doi.org/10.1016/j.actamat.2014.07.069.

[78] E. Sultan, A. Boudaoud, Statistics of crumpled paper, Phys. Rev. Lett. 96 (2006) 136103, http://dx.doi.org/10.1103/PhysRevLett.96.136103.

[79] A.S. Balankin, O.S. Huerta, Entropic rigidity of a crumpling network in a randomly folded thin sheet, Phys. Rev. E 77 (2008) 051124, http://dx.doi.org/10.1103/PhysRevE.77.051124.

[80] R. Lakes, Foam structures with a negative Poisson's ratio, Science 235 (1987) 1038–1040, http://dx.doi.org/10.1126/science.235.4792.1038.